PROCEEDINGS OF THE ROYAL SOCIETY A MATHEMATICAL, PHYSICAL & ENGINEERING SCIENCES

Hydrodynamic object recognition using pressure sensing

Roland Bouffanais, Gabriel D. Weymouth and Dick K. P. Yue

Proc. R. Soc. A 2011 **467**, 19-38 first published online 2 June 2010
doi: 10.1098/rspa.2010.0095

PROCEEDINGS OF THE ROYAL SOCIETY A

Proc. R. Soc. A (2011) **467**, 19–38
doi:10.1098/rspa.2010.0095
Published online 2 June 2010

Hydrodynamic object recognition using pressure sensing

By Roland Bouffanais*, Gabriel D. Weymouth and Dick K. P. Yue

Department of Mechanical Engineering, Massachusetts Institute of Technology, Cambridge, MA 02139, USA

Hydrodynamic sensing is instrumental to fish and some amphibians. It also represents, for underwater vehicles, an alternative way of sensing the fluid environment when visual and acoustic sensing are limited. To assess the effectiveness of hydrodynamic sensing and gain insight into its capabilities and limitations, we investigated the forward and inverse problem of detection and identification, using the hydrodynamic pressure in the neighbourhood, of a stationary obstacle described using a general shape representation. Based on conformal mapping and a general normalization procedure, our obstacle representation accounts for all specific features of progressive perceptual hydrodynamic imaging reported experimentally. Size, location and shape are encoded separately. The shape representation rests upon an asymptotic series which embodies the progressive character of hydrodynamic imaging through pressure sensing. A dynamic filtering method is used to invert noisy nonlinear pressure signals for the shape parameters. The results highlight the dependence of the sensitivity of hydrodynamic sensing not only on the relative distance to the disturbance but also its bearing.

Keywords: hydrodynamic mapping; pressure sensing; object detection and recognition

1. Introduction

The mechanosensory lateral line system (LLS) is a distributed, hair cell-based system which detects the fluid flow regime at the surface of most aquatic vertebrates, primarily fish and some amphibians. The LLS is composed of mechanosensory units called neuromasts, which occur free-standing on the skin (superficial neuromasts) or in fluid-filled canals (canal neuromasts) that open to the environment through a series of pores. The flow field around these aquatic vertebrates is perturbed by objects, peers and other living organisms present in the immediate vicinity. These hydrodynamic perturbations of both the pressure and velocity of the flow field are detected by the LLS and transduced into trains of nerve impulses which are transmitted to the central nervous system for post-processing. This provides the fish or the amphibian with some sort of hydrodynamic image of their surroundings (Bleckmann 1994; Coombs & Montgomery 1999; Montgomery *et al.* 2001; Coombs & Braun 2003).

*Author for correspondence (bouffana@mit.edu).

Received 17 February 2010
Accepted 5 May 2010

Despite its primitive nature, this unique distributed hydrodynamic sensing device is instrumental for many specific behaviours; for instance, prey detection, predator avoidance, schooling behaviour, courtship and spawning, rheotaxis, station holding and spatial orientation (Montgomery *et al.* 1997, 2002; Liao 2006, 2007).

Montgomery *et al.* (2001) reported the central role played by the LLS in the global sensory system of hypogean fishes, such as the Mexican blind cave fish (BCF). In the absence of light, the only sensory modality capable of providing detailed information of the surroundings is the LLS (Hensel 1978; Coombs & Montgomery 1999; Montgomery *et al.* 2001). Hydrodynamic sensing is conspicuous in the behaviour of the Mexican BCF. Experiments by von Campenhausen *et al.* (1981) and Burt de Perera (2004*b*) show that the Mexican BCF is not only able to detect the presence of obstacles placed in its environment, but, more astonishingly, it is capable of encoding both their shape and size given its hyperdeveloped mechanosensory LLS. Recently, Jamieson *et al.* (2009*a*,*b*) revealed the existence of swarms of hadal snailfish in one of the most inhospitable environments on the planet—in the Kermadec Trench at 7700 m below the Pacific Ocean surface. At this depth, such swarming behaviours certainly require a high level of distant touch hydrodynamic sensing. Given the harsh conditions, survival and feeding also require a high level of distant hydrodynamic imaging through pressure sensing, as hypothesized by Jamieson *et al.* (2009*a*).

To detect obstacles and to manoeuvre underwater, the vast majority of robots and vehicles rely primarily on acoustic and vision sensing. These traditional techniques have proved to be effective in the most commonly encountered configurations, but become inoperative in highly confined, turbid and murky environments. When considering autonomous underwater vehicles, manoeuvrability is often considered a more important design criterion than energy efficiency. Manoeuvrability requires acute sensing capabilities which can more easily be obtained through multi-modal sensory systems and devices. From the robotic standpoint, Fan *et al.* (2002) reported the first design and fabrication of an artificial lateral line flow sensor. Later, Yang *et al.* (2006) reported the first experimentations where such an artificial LLS is used to detect both a dipole and a wake, hence allowing it to mimic the pressure-sensing capabilities of those encountered in nature. Recently, McConney *et al.* (2009) reported yet another biologically inspired design of sensors showcasing more similarities with neuromasts than any other artificial devices before, and enhancing the detection of flow field perturbations.

Besides the mechanosensory lateral line, many fishes such as sharks, sturgeon and catfish are able to sense weak bioelectric fields emitted by aquatic prey through an electrosensory lateral line (ELL) system, leading to the so-called ‘passive electrolocation’. However, two specific groups of freshwater fish are capable of ‘active electrolocation’ as they both emit and sense an electric field, similar to active sensing systems such as radar and sonar (Nelson & MacIver 2006). Those active electrolocators can move around and hunt in total darkness just like BCF. Coombs *et al.* (2002) and Nelson *et al.* (2002) have compared the LLS and ELL, which exhibit many common features in both their structural and functional organization. According to Coombs *et al.* (2002), these two sensory systems appear to play similar roles in most of the specific behaviours mentioned above for the LLS exclusively. Despite this large body of

similarities, Coombs *et al.* (2002) also highlight the contrasting features of LLS versus ELL, which are primarily due to acute differences in the physical bases of mechanosensory and electrosensory stimuli as detailed in §2.

There is now accumulating evidence that superficial and canal neuromasts are distinctively used for specific behaviours. For instance, superficial neuromasts are essential to rheotaxis and station holding, while canal neuromasts are of prime importance in the obstacle detection and avoidance. Most experimental and theoretical studies on the LLS stimulus detection have focused on elucidating the encoding of the source distance and the encoding of the source location and direction (Coombs & Braun 2003). The vast majority of studies reported in the literature on these problems of detection and source encoding used a simple translating/vibrating sphere as a stimulus (e.g. the recent articles by Rapo *et al.* (2009) and Goulet *et al.* (2008) and the multiple references therein).

Despite the pervasive character of hydrodynamic sensing in nature and the growing body of cutting-edge biomimetic applications, the hydrodynamic fundamentals underpinning this sensory mode are still not clearly established. Windsor *et al.* (2008) have investigated the specific swimming kinematics of the Mexican BCF owing to its hydrodynamic imaging capability. Very recently, the foundations of hydrodynamic mapping using velocity sensing were laid by Sichert *et al.* (2009), in which vectorial velocity sensing was used to locate a moving disturbance and determine certain shape-scaling parameters. Fishes using canal neuromasts of LLS or an artificial sensing device, however, depend primarily on pressure sensing for fixed obstacle detection and identification (Coombs & Braun 2003; Yang *et al.* 2006). In addition, for any hydrodynamic mapping procedure to be general and viable, two key features are required. First, it has to be robust in the presence of a relatively high level of ubiquitous background noise (Coombs & Braun 2003). Second, the hydrodynamic mapping has to rely on a general shape representation to allow a complete sensitivity analysis (SA) to geometric characteristics of the disturbance over ranging distance and bearing.

2. Problem definition

For definiteness, consider the forward and inverse mapping problem for a BCF in a three-dimensional environment consisting of (vertical) column-like structures of unknown locations, sizes and cross-sectional geometries. This type of environment perfectly represents the fascinating tank experiment performed by S. Coombs (M. S. Triantafyllou 2008, personal communication). In the recorded movie of that experiment one can clearly observe a BCF swimming and finding its way through a Lego-brick maze. The BCF manages to avoid involuntary collisions with doors and obstacles and constantly maintains its swimming depth. Our choice of a three-dimensional environment with column-like structures aims at reproducing the environment sensed by the constant-depth swimming of the BCF. For typical BCF and/or structures of dimension of order ℓ with $\ell = 0.1\,\mathrm{m}$, and of speed of order one body length, ℓ, per second (Burt de Perera 2004*b*), viscous effects are relatively unimportant according to Triantafyllou *et al.* (2000). Thus, in this initial study, we ignore the vorticity shed by the obstacle and fish, and also the effects of the fish body/motion itself, and model the problem in the context of a two-dimensional potential flow.

The neglected effects can be readily accounted for later within the present framework. It must be added that the treatment of both the forward and inverse problems proposed in this article remains entirely valid with any possible flow, including the flow generated by the BCF itself while swimming. However, with such complex flows one has to resort to numerical simulations in order to access the solution of the forward problem unlike in the case considered here.

Specifically, this paper addresses the problem of a single body in the vicinity of the BCF. Our aim is to emphasize physical intuition and connections to the real-life biological systems through analytical analysis and results. The present results can be generalized to consider a multiple-body environment. The extension is particularly straightforward for multiple bodies sufficiently separated so that higher order hydrodynamic interactions can be neglected.

The problem we pose herein is decomposed into a forward and an inverse problem as follows. Pressure sensing is available over a finite, distributed and moving device (such as via an LLS of a fish or via an artificial sensory system of a vehicle) in the vicinity of a fixed solid obstacle, denoted by $\mathcal{O}_0$:

— given the location, size and shape characteristics of $\mathcal{O}_0$, determine the sensed pressure signature (the forward problem);
— given the sensed pressure signal (and a finite history of previously sensed pressures) determine the location, size and shape of $\mathcal{O}_0$ (the inverse problem).

Solving both the forward and inverse problems is instrumental in determining the shape discrimination capabilities of aquatic vertebrates/robots which rely on a mechanosensory LLS to build a map of their environment. The forward problem is by its very nature independent of the characteristics of the sensing device. On the other hand, the fact that the inverse problem is well posed and its solution is unique are strongly connected to the sensing mechanism and strategy. The general dependence of the properties of the inverse problem on the characteristics of the sensing device is, however, beyond the scope of the present study.

Modelling the pressure sensing after natural or artificial devices (Fan *et al.* 2002; Coombs & Braun 2003; Yang *et al.* 2006), we assume a finite noise-to-signal ratio γ in that measurement. This noise level primarily accounts for two sources of ubiquitous noise: the noise induced by the limited capabilities of the mechanotransducers forming the sensing device as well as the signal post-processing; and the background noise of the fluid flow in which the sensor is placed. The BCF itself is subject to the cumulative effects of these two main sources of noise and most likely to many other less intense sources.

Let the closed cross-section boundary of $\mathcal{O}_0$ be $\mathcal{C}$, and let $\mathcal{I}_S$ denote the sensed hydrodynamic image by the device. The perturbation caused by the presence of the obstacle is expressed mathematically as

$$\mathcal{I}_S = \mathcal{F}(\mathcal{C}), \tag{2.1}$$

where $\mathcal{F}$ is a nonlinear functional that depends on the fluid flow. In contrast to the active electrolocation discussed in §1, where the electric potential is governed by linear (Maxwell) equations, the hydrodynamic problem associated

with the functional $\mathcal{F}$ involves not only nonlinear governing equations but also the non-local relationship between the velocity and pressure fields. Thus, the mechanosensing forward and inverse problems are significantly more difficult than those using active electrosensing.

3. Obstacle shape characterization

In her seminal work about the encoding of geometric parameters by the BCF, Burt de Perera (2004*b*) highlights two important observations based on her multiple sets of behaviour experiments. First, her findings show the capability for a BCF to encode independently in its spatial map various geometric parameters including size, absolute distance to the obstacle and also the obstacle shape. Second, she concludes that, because of the fundamental limitations in distance over which the LLS can operate, the BCF can detect a change in distance despite not being able to perceive the whole environment at once. This compelling evidence is somehow counterintuitive from the human standpoint as we are used to perceiving the entire configuration of our environment at once through vision. The BCF perception of its environment appears to be extremely progressive. That progressive hydrodynamic imaging suggests that the BCF mental map accounts for the specific relationship between the distance with obstacles and its internal representation.

There is still no clear understanding of how the BCF builds its internal cognitive map of the environment it evolves in Burt de Perera (2004*a*). Given the limited computing and processing capabilities of any fish central nervous system, it is reasonable to assume that this cognitive map has to be built upon a compact representation of the environment. For the problem described in §2, our strategy is to relate the position/geometric characteristics of *any* body $\mathcal{O}_0$ to a general and unique mathematical representation in terms of (unknown) parameters. This representation must be in agreement with the two key observations of Burt de Perera (2004*b*) recalled above.

(*a*) *External conformal mapping*

As the set of two-dimensionally located shapes is inherently nonlinear and infinite dimensional, finding a simple way of representing and classifying its elements is key to determining an analytic solution of the forward problem. This is a non-trivial task (Sharon & Mumford 2006). In the present framework of two-dimensional potential flow, one powerful yet compact method is to conformally map the domain $\mathcal{D}$ exterior to the Jordan curve $\mathcal{C}$ (in z-space) onto the exterior of a disc (in ζ-space; see figure 1 for a schematic and a summary of notations)—generally not the unit disc (Nehari 1952). In our sensing problem, the domain $\mathcal{D}$ corresponds to the fluid domain surrounding the obstacle delimited by $\mathcal{C}$, which has to be detected and whose shape has to be discriminated. The Riemann mapping $\zeta = f(z)$ is unique and should be such that at infinity it behaves like the identical mapping; more precisely, the mapping function should have a simple pole at infinity and has a Laurent expansion which reads

$$\zeta = f(z) = z + b_0 + \frac{b_1}{z} + \frac{b_2}{z^2} + \ldots, \quad z \in \mathcal{D}. \tag{3.1}$$

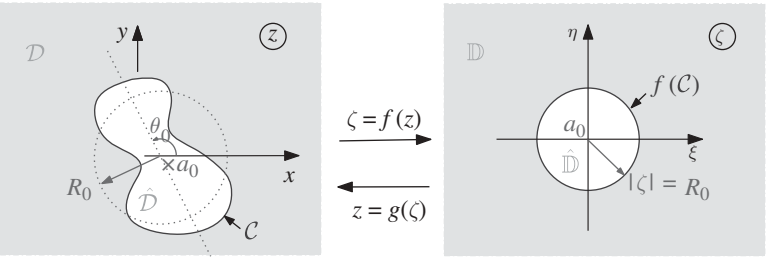

Figure 1. Schematic of direct and inverse mappings, and the internal and external domains. The set (a_0, R_0, θ_0) constitutes the three conformal elements associated with the external fluid domain $\mathcal{D}$.

For our study, the inverse exterior mapping $z = f^{-1}(\zeta) = g(\zeta)$ from the exterior of a disc onto the domain $\mathcal{D}$ is of practical interest. This mapping is conformal and its Laurent series

$$z = g(\zeta) = \zeta + a_0 + \frac{a_1}{\zeta} + \frac{a_2}{\zeta^2} + \ldots, \quad |\zeta| > R_0, \tag{3.2}$$

introduces two essential geometric quantities: R_0 and a_0, respectively, the uniquely defined (outer) conformal radius (Pólya & Szegö 1951) and the conformal centre (Pommerenke 1975; Duren 1983). The (external) conformal mapping provides a unique but not explicit definition of R_0 and a_0, which can be interpreted as the characteristic size and location of the obstacle.

Given the conformal centre a_0, the direct exterior mapping $\zeta = f(z)$ admits the following Laurent series centred at a_0

$$\zeta = f(z) = z - a_0 + \frac{b_1'}{z - a_0} + \frac{b_2'}{(z - a_0)^2} + \ldots, \quad z \in \mathcal{D}, \tag{3.3}$$

which simplifies the required inversion of the Laurent series (Morse & Feshbach 1953).

The conformal centre, $a_0 = -b_0$, may be calculated from the inverse mapping g by (Pommerenke 1975)

$$a_0 = \frac{1}{2\pi} \int_0^{2\pi} g(r\mathrm{e}^{\mathrm{i}\theta})\, \mathrm{d}\theta, \quad r > \mathrm{R}_0. \tag{3.4}$$

In practice, it can be estimated accurately by evaluating the inverse mapping g near infinity and subtracting off the known part of the series (3.2),

$$a_0 \simeq (g(\zeta) - \zeta)_{\zeta \to \infty}. \tag{3.5}$$

In general, the conformal centre is different from the centroid of the interior of the domain $\mathcal{D}$, although the difference is often small. The outer conformal radius R_0 should not be confused with the more commonly used inner conformal radius r_0. Indeed, unlike for the definition of r_0, the definition of R_0 does not involve a possibly varying point in $\mathcal{D}$ (Henrici 1974, 1986); the uniqueness of its definition is based on the choice of the point at infinity which is common to all exterior domains. It would be possible but totally inadequate to define an outer conformal radius based on another point in $\mathcal{D}$. There are several other approaches

to this same measure of the 'spread' of $\mathcal{D}$. For instance, the outer conformal radius is identical to the transfinite diameter (see Ahlfors 1973). Other approaches involve polynomial approximation (Chebyshev's constant) or potential theory (logarithmic capacity, Robin's constant); see Tsuji (1959) for greater detail. The outer conformal radius, like the transfinite diameter, the logarithmic capacity and the Robin's constant are all conformal invariants (Ahlfors 1973).

The shape representation is embodied in the inverse exterior Riemann mapping (3.2), and the governing equations for potential flow in z and ζ are conformally invariant. Indeed, potential flows are governed by a Laplace equation (Milne-Thomson 1968), which remains a Laplace equation through any change of variables associated with a conformal mapping. As we will show, the use of equation (3.2) allows one to separate the size/location of $\mathcal{O}_0$ from its shape characteristics (and a unique representation of the latter), leading to a powerful simplification of the general problem.

We remark that the central idea behind the use of the Laurent series is that shape information is indirectly encoded into the Laurent coefficients of the conformal mapping. This fact has been used for the mathematical description of two-dimensional Laplacian growth problems, such as the deterministic viscous fingering in a Hele–Shaw cell (Bazant & Crowdy 2005) and the stochastic diffusion-limited aggregation as modelled by Hastings & Levitov (1998) and Davidovitch *et al.* (1999). Bazant *et al.* (2003) used the encoding of morphological information in the Laurent coefficients of conformal mappings to study the dynamics of non-Laplacian growth phenomena. The reader is referred to the review by Bazant & Crowdy (2005) for details on the use of conformal mappings for both continuous and discrete growth problems. These mathematical concepts have also been used in a myriad of other fields where conformal mapping is applicable, such as in image recognition (Sharon & Mumford 2006).

(*b*) *Shape normalization and conformal elements*

If one considers various domains having the same shape, but shifted, dilated and rotated, it is possible to find a unique normalized inverse exterior mapping characterizing the shape only and defined as its fingerprint (Sharon & Mumford 2006). The normalization procedure consists of three basic steps in the complex plane: a translation of amplitude $-a_0$, followed by a dilation by a factor $1/R_0$ and finally a rotation about the origin by an angle $-\theta_0$. An arbitrary but unique choice of the value of the angle θ_0 is necessary to uniquely define the conformal axis of the shape. This latter quantity θ_0 associated with the conformal centre a_0 and radius R_0 constitute the so-called set of conformal elements of the located shape. Mathematically, the normalization leads to the definition of the shape fingerprint as an inverse exterior mapping, denoted by h, defined on the exterior of the unit disc

$$z = a_0 + R_0 \mathrm{e}^{\mathrm{i}\theta_0} h(\xi), \quad |\xi| > 1, \tag{3.6}$$

and admitting the following univalent Laurent series:

$$h(\xi) = \xi + \frac{\mu_1}{\xi} + \frac{\mu_2}{\xi^2} + \ldots, \quad |\xi| > 1, \tag{3.7}$$

where the coefficients $\{\mu_k\}_{k\geq 1}$ are explicitly related to the complex coefficients $\{a_k\}_{k\geq 1}$ appearing in equation (3.2), by

$$\mu_k = \frac{a_k}{(R_0 e^{i\theta_0})^{k+1}}, \tag{3.8}$$

and implicitly to the coefficients $\{b'_k\}_{k\geq 1}$ of the recentred forward mapping f (see equation (3.3)).

For any domain $\mathcal{D}$ different from the exterior of a disc,[1] the Laurent series (3.7) admits at least one non-zero coefficient, which is denoted μ_{k_0}. The angle θ_0 is chosen such that it is the smallest angle enforcing that μ_{k_0} is real and positive. In the trivial case of a circular shape, the value of the angle θ_0 is logically set to zero. In the simple case where $a_1 \neq 0$ and $a_k = 0$ for all $k \geq 2$ in the Laurent expansion (3.2), the obstacle has an elliptic cross section. The corresponding ellipse is centred at a_0 with its major axis turned about a_0 by an angle equal to $\arg(a_1)/2$ with respect to the x-axis. The conformal radius R_0 has a clear geometric meaning in this particular case, being the arithmetic mean of the semi-minor and semi-major axes of the ellipse.

The analytic function h is, by definition, univalent (Pommerenke 1975; Duren 1983) and consequently satisfies theorems such as the so-called one-fourth theorem and the area theorem (Krantz 1999), hence imposing constraints on the coefficients $\{\mu_k\}_{k\geq 1}$ of the shape fingerprint, for instance

$$|\mu_k| \leq \frac{1}{\sqrt{k}}, \quad k \geq 1. \tag{3.9}$$

The normalization procedure represented by equation (3.6) gives access to the set of conformal elements and the fingerprint h, providing a unique and complete characterization of *any* located body $\mathcal{O}_0$. Each term in $1/\xi^k$ in the Laurent series (3.7) has a clear geometric meaning and is associated with a polygonal type of perturbation of the unit circle; more precisely, a $(k+1)$-gonal type perturbation also referred to as non-self-intersecting hypotrochoids or order k (Muskhelishvili 1963). For example, the leading terms in $1/\xi$ and $1/\xi^2$ correspond, respectively, to a digonal[2] and an equilateral triangle (or trigonal) type of perturbation.

The essential difference between the set of conformal elements and the shape fingerprint is that the former are independent of the distance from which the shape is observed. Given the noise-to-signal ratio γ, and the relative distance to the body δ defined by

$$\delta = \frac{|z - a_0|}{R_0} = |h(\xi)|, \tag{3.10}$$

only a certain number of terms are necessary in the asymptotic series (3.7) to fully represent a located shape. This fact is central to the present problem of shape detection and discrimination through pressure sensing.

The above shape representation exhibits the two central features reported by Burt de Perera (2004*a*). First, the progressive character of the mapping process due to the limited perceptual range of the BCF. This is fully characterized by the fact that the shape fingerprint is represented by an asymptotic Laurent expansion

[1]This trivial case corresponds to $\mu_k = 0$ for all $k \geq 1$.
[2]Degenerate polygon with only two vertices.

(see equation (3.7)) associated with the mathematical properties discussed above. The progressive discrimination of the shape is indeed highly dependent on the relative distance δ to the obstacle and the noise-to-signal ratio γ, which condition the necessary number of terms in the asymptotic expansion of the fingerprint. This aspect is further discussed and exemplified in §3*c*. Second, the normalization procedure allows one to independently encode the size, location and shape parameters just as BCF do. Let $\mathcal{N} = \{a_0, R_0, \theta_0\}$ denote the set of conformal elements and $\mathcal{S} = \{\mu_k\}_{k\geq 1}$ the set of shape coefficients associated with the fingerprint representation (3.7). The fundamental governing equation (2.1) of the forward and inverse problems can therefore be cast as

$$\mathcal{I}_S = \mathcal{F}(\mathcal{N}, \mathcal{S}). \tag{3.11}$$

This reformulation of the problem suggests a two-step approach to tackle the inverse problem where $\mathcal{N}$ and $\mathcal{S}$ are sought independently. This approach is considered in the sequel together with an analysis of which of the two sets, $\mathcal{N}$ or $\mathcal{S}$, should be determined first (see §§4 and 5).

We remark finally that the detailed shape representation introduced here in a two-dimensional framework for simplicity can be generalized to three-dimensional problems. Indeed, similar representations exist in three dimensions and have been reported in the literature (Rothe *et al.* 1996). In fact, all the discussion associated with our two-dimensional representation, and its relevance with respect to the BCF mapping behaviour, remains valid for its three-dimensional counterpart.

(*c*) *Model description*

To exemplify the mathematics underlying the description of this physical problem, a model of biological relevance is devised based on physical parameters encountered in a typical BCF (*Astyanax mexicanus*) of head-to-tail length ℓ. The BCF is placed in an unbounded environment (dimensions greater than $\mathcal{O}(100\ell)$) wherein lies a single solid obstacle $\mathcal{O}_0$ of characteristic length given by its outer conformal radius, $R_0 = \ell$. Given our assumptions discussed in §2, the fish is neither generating nor perturbing the flow, which is set to a magnitude $U_\infty = \ell/\mathrm{s}$ corresponding to the average swimming speed of the BCF (Burt de Perera 2004*b*) of approximately a body length ℓ per second. The obstacle $\mathcal{O}_0$ is conformally centred ($a_0 = 0$) and conformally oriented ($\theta_0 = 0$). Its shape fingerprint, characterized by the univalent mapping h, is chosen to display both a round and a pointed end, as depicted in figure 2*d*. Such a normalized shape is obtained by specifying the following values:

$$\mu_1 = \tfrac{1}{3}, \quad \mu_2 = \tfrac{1}{6}, \quad \mu_3 = \tfrac{1}{12}, \quad \mu_k = 0 \quad \text{for } k \geq 4,$$

for the complex coefficients appearing in the asymptotic Laurent expansion (3.7).

The shape construction process of the obstacle $\mathcal{O}_0$ is highlighted in figure 2. This process starts from the unit circle $z = \xi$ in figure 2*a* which is perturbed by the digonal term $1/(3\xi)$. This first additional term has the effect of flattening the unit circle in the direction given by the argument of $\mu_1 = \frac{1}{3}$, which corresponds here to the x-axis; hence, leading to an elliptical shape represented in figure 2*b*. Subsequently, the shape (figure 2*b*) is perturbed by an equilateral triangular term, μ_2/ξ^2, leading to the appearance of three bumps in figure 2*c* in the three

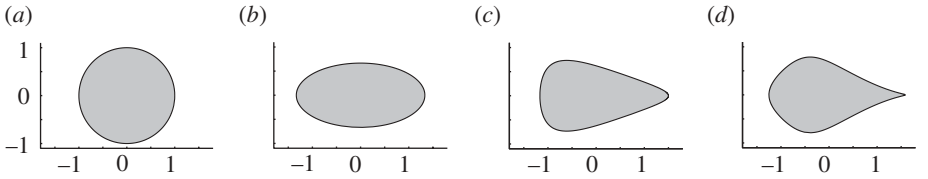

Figure 2. Conformal images of the outer unit disc with increasingly higher terms: (*a*) $z=\xi$; (*b*) $z=\xi+1/(3\xi)$; (*c*) $z=\xi+1/(3\xi)+1/(6\xi^2)$; and (*d*) the shape fingerprint $z=h(\xi)=\xi+1/(3\xi)+1/(6\xi^2)+1/(12\xi^3)$.

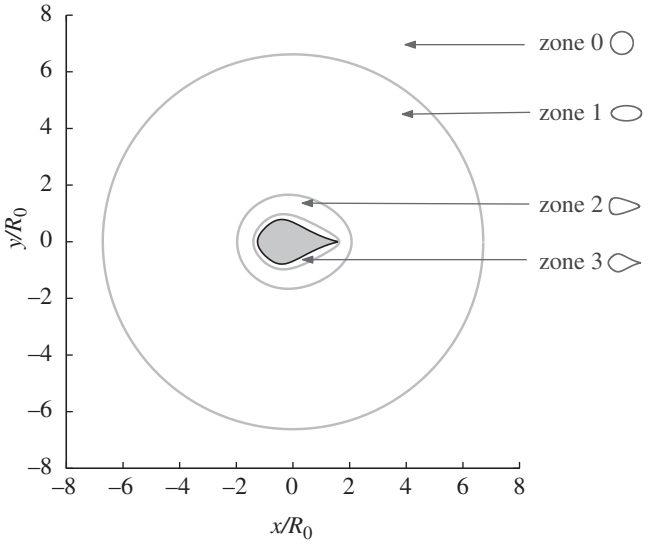

Figure 3. Geometrical map of the progressive shape discrimination. The different zones are obtained for a residual parameter $\varepsilon=5\%$ in the asymptotic series (3.7) representing the shape fingerprint.

principal directions. Ultimately, the shape (figure 2*c*) is perturbed by a square term, μ_3/ξ^3, leading to the actual fingerprint figure 2*d*, which presents both a round and a pointed end along the x-axis.

The fingerprint being an asymptotic series, the shape-building process (a)→(d) genuinely represents the physical dynamic deblurring effect felt by the BCF (with finite γ) when it approaches the obstacle from far away in any direction. As discussed in §3*b*, this progressive hydrodynamic imaging of the obstacle is typical of the BCF behaviour due to the natural limitations of the LLS perceptual range (Burt de Perera 2004*b*). Without needing to resort to a complete hydrodynamic analysis of the flow, it is clear that the actual shape (figure 2*d*) is first 'perceived' as a circle (figure 2*a*), and subsequently as an ellipse (figure 2*b*), then as figure 2*c* and ultimately as it is (figure 2*d*). The geometrical map of the progressive shape discrimination is shown in figure 3. This map must not be confused with the actual map obtained when sensing pressure through the LLS. However, it illustrates

perfectly the central concept of progressive shape discrimination. The transition between successive perceptual zones $(k-1)\to k$ occurs when the polygonal term $|\mu_k/\xi^k|<\varepsilon$, where ε is the maximum residual parameter in the asymptotic series (3.7). The transitions between these zones depend both on the direction of approach and on the value of ε. This conclusion remains valid for the actual physical map based on pressure sensing by exchanging ε with the noise level γ. These transitions for the physical map are fully determined when solving the forward problem.

4. Forward problem

Prior to tackling the inverse problem, we first solve the forward problem where the exact description is available analytically to any order.

(*a*) *Pressure field*

For definiteness, we assume an imposed uniform external flow $\mathbf{U}=U_\infty\hat{\mathbf{e}}_\alpha$ making an angle α with the x-axis. The complex potential w is obtained through conformal mapping (Milne-Thomson 1968)

$$w=U_\infty\left[\zeta\mathrm{e}^{-\mathrm{i}\alpha}+\frac{R_0^2\mathrm{e}^{\mathrm{i}\alpha}}{\zeta}\right],\quad |\zeta|>R_0, \tag{4.1}$$

where $\zeta=f(z)$ is the Laurent series (3.1) rewritten as centred at the conformal centre a_0 as in equation (3.3). To express the complex potential (4.1) in the physical plane in terms of z and the obstacle geometric characteristics $\mathcal{N}=\{a_0,R_0,\theta_0\}$ and $\mathcal{S}=\{\mu_k\}_{k\geq1}$, a series inversion up to a given order (Morse & Feshbach 1953) of the Laurent expansion (3.2) is required. This inversion process is mathematically guaranteed by the univalent fingerprint h and the form of its Laurent series (Pommerenke 1975; Duren 1983). It yields the expression of the coefficients $\{b'_k\}_{k\geq1}$ appearing in equation (3.3) in terms of $\{a_k\}_{k\geq1}$ which embody both $\mathcal{S}$ and $\{R_0,\theta_0\}$. The conformal centre a_0, which completes the set $\mathcal{N}$, appears explicitly in the asymptotic series (3.3). This inversion allows us to express the pressure field p as

$$p(z)=P_\infty-\frac{1}{2}\rho\left|\frac{\mathrm{dw}}{\mathrm{dz}}\right|^2, \tag{4.2}$$

with $P_\infty=p_\infty+\rho U_\infty^2/2$, and p_∞ being the pressure at infinity and ρ the fluid density. Assuming that the smallest term in the shape fingerprint (3.7) is of order n, then the highest order term in the asymptotic series giving the pressure field is of order $2(n+1)$. With a noise level of, say, $\gamma=\mathcal{O}(10\%)$, it suffices to consider the first three terms in $1/\xi$ in the shape fingerprint h corresponding, respectively, to a digon, an equilateral triangle and a square type of perturbation. Indeed, the first neglected term for the relative pressure is of the order of $1/\delta^9$. Posing $Z=(z-a_0)\mathrm{e}^{-\mathrm{i}\alpha}/R_0$, the inversion of the series up to that order gives

$$w=U_\infty R_0\left[Z+\frac{\varpi_1}{Z}+\frac{\varpi_2}{Z^2}+\frac{\varpi_3}{Z^3}\right]+\mathcal{O}\left(\frac{1}{Z^4}\right), \tag{4.3}$$

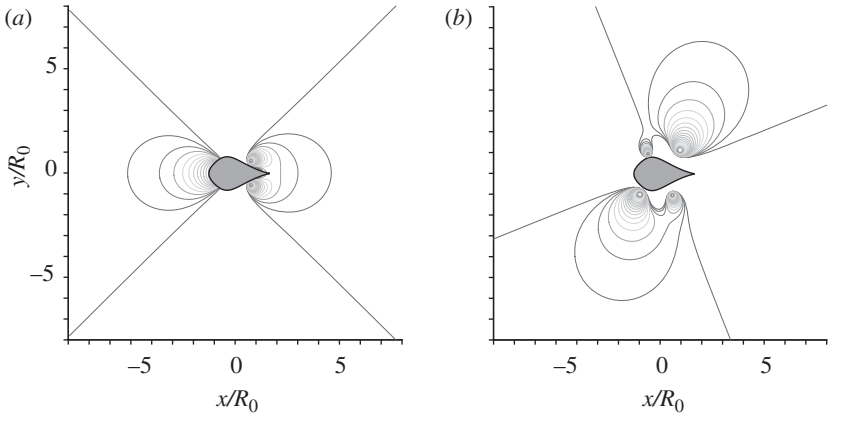

Figure 4. Contours of the relative pressure field $(p - P_\infty)/(-\rho U_\infty^2/2)$ obtained from equation (4.4) around the obstacle $\mathcal{O}_0$. The plot comprises 20 evenly distributed contours ranging from 0 to 1. Two angles α for the imposed external flow at infinity are considered: (a) $\alpha = 0$ and (b) $\alpha = \pi/3$.

with $\varpi_1 = 1 - \mu_1 e^{2i(\theta_0-\alpha)}$, $\varpi_2 = -\mu_2 e^{3i(\theta_0-\alpha)}$ and $\varpi_3 = \mu_1 e^{2i(\theta_0-\alpha)} - (\mu_1^2 + \mu_3)e^{4i(\theta_0-\alpha)}$. Ultimately,

$$p = P_\infty - \frac{\rho U_\infty^2}{2}\left|1 - \frac{\varpi_1}{Z^2} - \frac{2\varpi_2}{Z^3} - \frac{3\varpi_3}{Z^4}\right|^2 + \mathcal{O}\left(\frac{1}{\delta^9}\right) \tag{4.4}$$

is the pressure field in terms of the characteristics of the prescribed flow $\mathbf{U} = (U_\infty, \alpha)$ and of the obstacle $\mathcal{C} = (\mathcal{N}, \mathcal{S}) = (a_0, R_0, \theta_0, \{\mu_k\}_{k\geq 1})$. Contour plots of the distribution of the pressure field are shown in figure 4 for two different directions of the externally imposed flow, $\alpha = 0$ and $\alpha = \pi/3$. Note that, in the close vicinity of the obstacle $\mathcal{O}_0$, the expression (4.4) ceases to be valid owing to a lack of higher order terms.

The expression (4.4) governs the forward problem of hydrodynamic mapping through pressure sensing.

One should note the different dependencies of the pressure field on the conformal elements. On the one hand, a_0 and R_0 appears only indirectly through the reduced variable $Z = (z - a_0)e^{-i\alpha}/R_0$. On the other hand, the conformal orientation θ_0 plays a role in every single coefficient $\{\varpi_k\}_{k=1,2,3}$. This distinctive role played by θ_0 influences the directional character of the inverse hydrodynamic pressure-sensing problem, as will be shown in §5.

(b) *Radial distance SA*

Given the general conformal shape representation adopted and its fundamental properties of perceptual shape discrimination and independent determination of size, location and shape, our approach makes possible a general SA of hydrodynamic mapping. Such a general SA is not readily available, for example, within the multipole expansion framework of Sichert *et al.* (2009). Note that we consider here hydrodynamic mapping based on a fixed single-point pressure-sensing device. We expect the results of this SA based on a fixed single-point pressure sensing to be more restrictive than those

obtained with a moving and/or multi-point pressure-sensing device. However, these results will still inform possible approaches to the solution of the inverse problem.

Equation (4.4) is the nonlinear functional equation $\mathcal{I}_S = \mathcal{F}(\mathcal{C}) = \mathcal{F}(\mathcal{N}, \mathcal{S})$ to be inverted when sensing hydrodynamically. More precisely, the hydrodynamic image $\mathcal{I}_s$ is simply the local value of the pressure field p as single-point pressure sensing is considered. This SA is instrumental to identifying the level of uncertainty associated with each unknown geometric parameter depending on the relative distance $\delta = |Z|$ to the obstruction. Independent local perturbation analyses are made possible owing to the independent representation of each geometric parameter in $\mathcal{N}$ and $\mathcal{S}$, as detailed in §3*b*.

These perturbation analyses show that the normalizing conformal elements $\mathcal{N} = \{a_0, R_0, \theta_0\}$ have their highest correction term varying in $1/\delta^3$, $1/\delta^2$ and $1/\delta^2$, respectively. This highlights an instrumental feature of hydrodynamic mapping based on single-point pressure sensing: the mapping procedure exhibits a lower sensitivity in positioning the obstacle relative to its sizing, scaling or orientating.

Similarly, independent perturbation analyses of equation (4.4) reveal the sensitivity in determining the shape coefficients $\mathcal{S}$ through pressure sensing with respect to the relative distance δ to the obstacle. Not surprisingly, we find that perturbations of $\{\mu_k\}_{k\geq 1}$ result in correction terms of order $1/\delta^{k+1}$. In other words, the final pressure solution is progressively less sensitive to each perturbation. These conclusions for the shape fingerprint coefficients $\mathcal{S}$ are in total agreement with the results of our simplified analysis of the progressive shape discrimination based only on the geometric shape fingerprint representation presented in §3*c*.

(*c*) *Pressure nodal lines*

The SA presented in §4*b* reveals instrumental features of hydrodynamic mapping through pressure sensing, though limited to the influence of the distance to the object to detect and discriminate. However, the directionality of the mapping process has been highlighted at the end of §4*a*. It seems therefore natural to extend the SA to account for the sensitivity of the pressure distribution to the relative angular variable (with respect to the direction of the imposed external flow) defined as

$$\Theta = \arg(Z) = \arg(z - a_0) - \alpha = \theta - \alpha. \tag{4.5}$$

At sufficiently large distance δ, equation (4.4) becomes

$$\frac{p - P_\infty}{-\rho U_\infty^2/2} = 1 - \frac{2|\varpi_1|}{\delta^2}\cos(2\Theta - \Phi_1) + \frac{|\varpi_1|^2}{\delta^4}, \tag{4.6}$$

with $\Phi_1 = \arg(\varpi_1) = \arg(1 - \mu_1 \mathrm{e}^{2\mathrm{i}(\theta_0 - \alpha)})$ depending explicitly on the shape coefficient μ_1 but also on the relative orientation of the obstacle (through its conformal orientation) to the direction of the perturbing external flow. If one approaches $\mathcal{O}_0$ along a constant Θ_1 line such that $\cos(2\Theta_1 - \Phi_1)$ vanishes, then, instead of gathering information in the $1/\delta^2$ range, one would only receive the information scaled by $1/\delta^4$ (which may fall into the noise level). Such angles Θ_1 are 'nodes' in the pressure information for the digonal fingerprint perturbation, and the difficulty of the inversion is greatly increased if sampling occurs only in the vicinity of such nodal lines.

Similar comments apply to the higher order terms involving vanishing terms with the general form $\cos((k+1)\Theta_k - \Phi_k)$ with $\Phi_k = \arg(\varpi_k)$, thus yielding an increasingly higher number of (higher order) nodal lines. As mentioned for Θ_1, the values of Θ_k depend exclusively on the body shape and (relative) bearing $(\theta_0 - \alpha)$, and it is important to stress that they are not known *a priori*.

(*d*) *Progressive perceptual zoning*

As a final step in the study of the forward problem, we discuss the progressive perceptual zoning based on single-point pressure sensing. To this aim, we assume that the normalizing conformal elements $\mathcal{N}$ have already been determined. This problem is considered in a simplified framework in §3*c*, where the progressive shape discrimination capabilities are analysed based purely on geometric arguments. The objective now is to determine the physical map equivalent to the geometrical map shown in figure 3. The definitions of the zones $0 \to 3$ remain the same as the one used in figure 3, i.e. zone k is the part of the fluid domain where the shape discrimination is possible up to the term of order k associated with the coefficient μ_k.

Based on the expression (4.4) of the pressure field in the fluid domain surrounding the obstacle $\mathcal{O}_0$, we can have access to the sensed pressure at any point in zone 3 where the shape of $\mathcal{O}_0$ is completely discriminated. Zone 2 is defined by

$$\left| \frac{p(z;\mathcal{N};\mu_1,\mu_2,\mu_3) - p(z;\mathcal{N};\mu_1,\mu_2,\mu_3=0)}{p(z;\mathcal{N};\mu_1,\mu_2,\mu_3=0)} \right| \geq \epsilon, \tag{4.7}$$

and the frontier with zone 3 corresponds to the equality. Similarly zone 1 and its frontier with zone 2 are given by

$$\left| \frac{p(z;\mathcal{N};\mu_1,\mu_2,\mu_3) - p(z;\mathcal{N};\mu_1,\mu_2=0,\mu_3=0)}{p(z;\mathcal{N};\mu_1,\mu_2=0,\mu_3=0)} \right| \geq \epsilon, \tag{4.8}$$

and between zone 1 and zone 0

$$\left| \frac{p(z;\mathcal{N};\mu_1,\mu_2,\mu_3) - p(z;\mathcal{N};\mu_1=0,\mu_2=0,\mu_3=0)}{p(z;\mathcal{N};\mu_1=0,\mu_2=0,\mu_3=0)} \right| \geq \epsilon. \tag{4.9}$$

The value of the parameter ϵ is associated with both the sensitivity level of the single-point pressure sensor and the noise-to-signal ratio γ.

Based on these definitions of the zoning, the map of progressive perceptual pressure sensing is shown in figure 5. The zoning clearly shows the fairly short-range character of the shape discrimination based on pressure sensing. This fact has been well known for a long time in the context of the obstacle detection problem (von Campenhausen *et al.* 1981; Coombs & Montgomery 1999; Goulet *et al.* 2008). However, the present results extend these earlier results to the obstacle shape discrimination problem in a quantitative way: to determine the shape coefficient μ_1 (resp. μ_2) it is required to perform sensing in a range $\simeq 3R_0$ (resp. $\simeq R_0$). The determination of a higher order shape coefficient—for instance μ_3 in our model—requires sensing extremely close to and almost in contact with the obstacle. These results are in agreement with the conclusions of our SA for the shape coefficients presented in §4*b*. The map in figure 5 also highlights a singular difference with the geometrical map

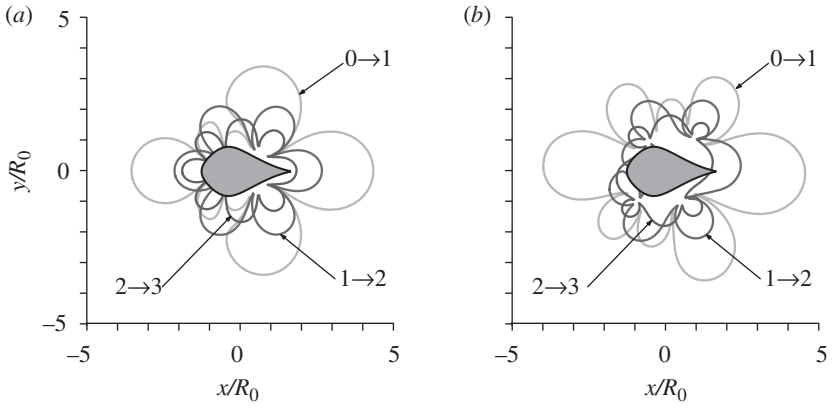

Figure 5. Zoning of the progressive perceptual shape discrimination based on single-point pressure sensing. The frontiers are given by equations (4.7)–(4.9) with $\epsilon = 5\%$ for two different directions of the imposed external flow: (*a*) $\alpha = 0$ and (*b*) $\alpha = \pi/3$.

in figure 3. The high-sensitivity zones of shape discrimination are made of directional lobes separated by the set of nodal lines introduced in §4*c*. This is a further confirmation of the high directionality in shape detection through pressure sensing.

Given the above forward analysis of the problem, we conclude that practical shape discrimination, i.e. the inverse problem, based solely on static single-point pressure sensing is simply not effective. One has to be so close and properly oriented to have a slight chance of even detecting the lowest shape coefficients. To overcome these serious constraints and extend the range of shape discrimination, it is necessary to resort to a dynamically moving multi-point sensory device such as the LLS. Our investigation of the inverse problem in the next section builds upon these two requirements.

5. Inverse problem analysis

The objective in the sequel is to assess and demonstrate the invertibility of the functional (4.4) based on the strategy proposed at the end of §4*d*. Hence, we consider a sensor array providing a distributed set of pressure data and moving along different possible paths.

(*a*) *Inversion methodology*

To approximately model the experience of the BCF, the sensor data are assumed to be noisy and only given over the (small) length of a sensor array. The array is arbitrarily prescribed as 11 single-point sensors evenly distributed along a circle, providing the noisy average signal at the array centroid as input for inversion. There is no doubt that the design of the sensor array plays a central role in the optimization of the inversion procedure. Moreover, the choice of the path followed by the sensor array as it moves in time during the dynamic inversion also has a central importance in the optimization of the whole process. However,

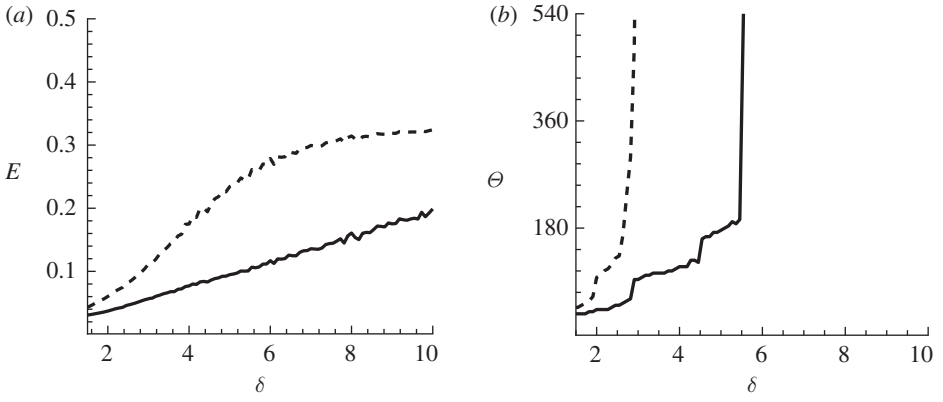

Figure 6. Characteristics of inverting the conformal centre a_0 (dashed line) and radius R_0 (solid line) along circular paths at scaled distance δ. (a) Error after 1.5 revolutions (540°). (b) Required arc of travel to reduce error to γ. Results for $\gamma = 10\%$ and $\alpha = 0$.

our study aims at obtaining a proof of feasibility for the inversion procedure. The optimal sensor array design and path followed represent new and exciting areas for future study.

An exact inversion is not possible for the test problem considered because the data are incomplete and corrupted, and, as equation (4.4) shows, the process of generating the pressure from the geometric parameters is highly nonlinear. Instead of an exact inversion, the goal is to determine the dependence of the inversion accuracy on the distance and orientation of the obstruction in order to establish the connection with the radial and angular SA presented in §4. To this end, the sensor device is moved along two types of predetermined paths: concentric circles centred at the obstacle, and ray lines converging on the obstacle. The pressure signals are generated through use of equation (4.4) with an added noise. In sensory ecology, noise can generally be assumed to be random fluctuations with a normal distribution (Dusenbery 1992). In the sequel, the background noise is considered to have a normal distribution fully characterized by γ. The estimated geometric properties are initialized with 100 per cent error and updated iteratively at each time step with an unscented Kálmán filter, a robust dynamic probabilistic signal filtering technique for highly nonlinear systems (Julier & Uhlmann 2004).

Following the results of the SA in §4*b* with respect to the relative distance δ to the obstacle, we adopt a hierarchical approach in which normalizing coefficients $\mathcal{N}$, i.e. the location and size in this case, are first determined. Once these coefficients are known with sufficient confidence, we subsequently focus on discriminating the shape of $\mathcal{O}_0$.

(*b*) *Location and size detection*

Figure 6 shows the characteristics for inverting the conformal centre a_0 and radius R_0 of the obstacle $\mathcal{O}_0$. In figure 6*a* the error E in the estimated parameters is shown after travelling 1.5 revolutions around the disturbance at a relative distance $\delta = |Z|$. The results show a steady increase in accuracy in both centre

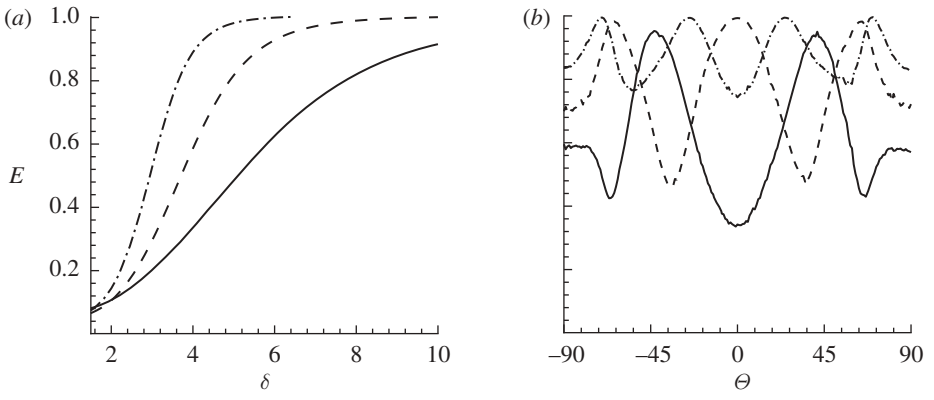

Figure 7. Characteristics of inverting the shape fingerprint coefficients μ_1 (solid line), μ_2 (dashed line) and μ_3 (dash-dotted line). (*a*) Error after 1.5 revolutions (540°) at distance δ. (*b*) Error after travelling from $\delta = 10 \rightarrow 2$ along approach angle Θ. Results for $\gamma = 10\%$ and $\alpha = 0$.

and radius inversion with proximity of the sensor to the disturbance, as well as the higher accuracy of the radius inversion compared with the centre inversion at any distance.

These results are in agreement with the conclusions of the SA and are further illustrated in figure 6*b*, which shows the arc of travel Θ around the disturbance required to drive the error below the noise level. The required arc increases with increased distance and asymptotes to infinity at $\delta \simeq 6$ for the R_0 inversion and $\delta \simeq 3$ for the a_0 inversion. Beyond these distances the conformal centre and radius cannot be inverted accurately regardless of the path length. These conclusions are in agreement with the previous experimental and numerical analyses of this problem (von Campenhausen *et al.* 1981; Coombs & Montgomery 1999; Goulet *et al.* 2008).

(*c*) *Shape discrimination*

After determining the location and size of the obstacle with the maximum accuracy possible (given the finite level of noise), we follow the hierarchical inversion approach and seek to discriminate the shape.

Figure 7 shows inversion characteristics for the fingerprint parameters (μ_1, μ_2, μ_3) of the flow disturbance $\mathcal{O}_0$. The true fingerprint matches the shape in figure 2*d*, and figure 7*a* shows the error E in each parameter after 1.5 revolutions around $\mathcal{O}_0$ at a distance δ. As predicted by the radial SA in §4*b* and by the study of the progressive perceptual zoning in §4*d*, the higher order terms require greater proximity to achieve any given error level owing to the more rapid attenuation of the relevant portion of the pressure signal. Not surprisingly, the present moving multi-point sensory device requires less proximity to capture each individual shape coefficient. For instance, the progressive perceptual zoning shown in figure 5 highlights the quasi impossibility of accessing the coefficient μ_3 unless one is almost in contact with $\mathcal{O}_0$. Figure 7*a* proves that μ_3 can be determined with reasonable accuracy in the range $\delta \simeq 2$ by resorting to our (non-optimized) inversion methodology.

Our study of the forward problem in §4*c* reveals the high directionality and the existence of pressure nodal lines for the inverse problem. These nodal lines are shown in the progressive perceptual zoning study in §4*d*. Figure 7*b* shows the error after travelling towards the object from a distance of $\delta = 10$ to 2 at different approach angles Θ. As expected from the forward analysis of the problem, there are distinct nodal lines along which the inversion is highly unreliable. The number and spacing of the Θ_k-nodes are in agreement with the values corresponding to vanishing $\cos((k+1)\Theta_k - \Phi_k)$. We conclude that this is a non-obvious but fundamental limitation in hydrodynamic mapping using pressure sensing.

6. Conclusions

In this article, a general obstacle representation based on normalization through conformal mapping is used to account for the specific features of progressive perceptual hydrodynamic imaging reported experimentally. For instance, the normalizing coefficients (size, location and orientation) and the shape ones are all encoded separately, which is recommended when considering an incremental inversion. The shape representation rests upon an asymptotic series which embodies the progressive character of hydrodynamic imaging through pressure sensing.

This general representation is employed to study the forward problem and to express analytically the pressure disturbance generated by a general parameterized object in a background flow. The pressure disturbance is used to analyse the efficacy of a hydrodynamic sensing system such as the LLS. The forward problem analysis allows us to obtain a general SA of the pressure-based hydrodynamic sensing. This SA is supplemented by a characterization of the progressive perceptual zoning which reveals that static single-point pressure sensing is ineffective when it comes to discriminating shapes.

Considering a moving multi-point sensing device, we investigate the inverse problem of hydrodynamic imaging. A dynamic hierarchical approach strategy using an LLS to build a map of a flow environment is suggested by our analysis. First, in the long-distance range, the objective is to obtain the best normalization parameters attainable, which is only possible by moving towards the disturbance. In agreement with the analysis of Sichert *et al.* (2009) and biological findings (Coombs & Braun 2003), the sensor must approach to within a short distance of the disturbance (approx. $3R_0$) to accurately establish its location. The second step is to discriminate the shape fingerprint, which requires the sensor to circle around the obstruction. Indeed, the very existence of the nodal lines prevents a purely radial straight-line approach to hydrodynamic mapping using pressure information, favouring instead a circular approach to confidently acquire the parameters μ_k.

These findings seem to explain the documented 'accelerate and glide past' behaviour of BCF when placed in the presence of a new obstacle (von Campenhausen *et al.* 1981) and suggest that man-made vehicles using pressure sensing for hydrodynamic mapping should probably adopt similar strategies.

The authors would like to thank Prof. Michael Triantafyllou and Mr Vicente Fernandez for insightful discussions. This work is supported by grants from ONR, and by a Swiss National Science Foundation fellowship no. PBELA–118718 (for R.B.).

References

Ahlfors, L. V. 1973 *Conformal invariants*. London, UK: McGraw-Hill.

Bazant, M. Z. & Crowdy, D. 2005 Conformal mapping methods for interfacial dynamics. In *Handbook of materials modeling* (ed. S. Yip), ch. 4, pp. 1417–1451. Berlin, Germany: Springer.

Bazant, M. Z., Choi, J. & Davidovitch, B. 2003 Dynamics of conformal maps for a class of non-Laplacian growth phenomena. *Phys. Rev. Lett.* **91**, 045503. (doi:10.1103/PhysRevLett.91.045503)

Bleckmann, H. 1994 *Reception of hydrodynamics stimuli in aquatic and semiaquatic animals*. New York, NY: Fischer.

Burt de Perera, T. 2004*a* Fish can encode order in their spatial map. *Proc. R. Soc. Lond. B* **271**, 2131–2134. (doi:10.1098/rspb.2004.2867)

Burt de Perera, T. 2004*b* Spatial parameters encoded in the spatial map of the blind Mexican cave fish, *Astyanax fasciatus*. *Anim. Behav.* **68**, 291–295. (doi:10.1016/j.anbehav.2003.11.009)

Coombs, S. & Braun, C. B. 2003 Information processing by the lateral line system. In *Sensory processing in aquatic environments* (eds S. P. Collin & N. J. Marshall), ch. 7, pp. 122–138. Berlin, Germany: Springer.

Coombs, S. & Montgomery, J. C. 1999 The enigmatic lateral line system. In *Comparative hearing: fish and amphibians* (eds R. R. Fay & A. N. Popper), pp. 319–362. Springer Handbook of Auditory Research. New York, NY: Springer.

Coombs, S., New, J. G. & Nelson, M. 2002 Information-processing demands in electrosensory and mechanosensory lateral line systems. *J. Physiol. Paris* **96**, 341–354. (doi:10.1016/S0928-4257(03)00013-5)

Davidovitch, B., Hentschel, H. G. E., Olami, Z., Procacia, I., Sander, L. M. & Somfai, E. 1999 Diffusion limited aggregation and iterated conformal maps. *Phys. Rev. E* **59**, 1368–1378. (doi:10.1103/PhysRevE.59.1368)

Duren, P. L. 1983 *Univalent functions*. Heidelberg, Germany: Springer.

Dusenbery, D. B. 1992 *Sensory ecology*. New York, NY: W.H. Freeman and Co.

Fan, Z., Chen, J., Zou, J., Bullen, D., Liu, C. & Delcomyn, F. 2002 Design and fabrication of artificial lateral line flow sensors. *J. Micromech. Microeng.* **12**, 655–661. (doi:10.1088/0960-1317/12/5/322)

Goulet, J., Engelmann, J., Chagnaud, B. P., Franosch, J. M. P., Suttner, M. D. & van Hemmen, J. L. 2008 Object localization through the lateral line system of fish: theory and experiment. *J. Comp. Physiol. A* **194**, 1–17. (doi:10.1007/s00359-007-0275-1)

Hastings, M. B. & Levitov, L. S. 1998 Laplacian growth as one-dimensional turbulence. *Physica D* **116**, 244–252. (doi:10.1016/S0167-2789(97)00244-3)

Henrici, P. 1974 *Applied and computational complex analysis: power series—integration—conformal mapping—location of zeros*, vol. 1. New York, NY: Wiley-Interscience.

Henrici, P. 1986 *Applied and computational complex analysis: discrete Fourier analysis—Cauchy integrals—construction of conformal maps—univalent functions*, vol. 3. New York, NY: Wiley-Interscience.

Hensel, K. 1978 Morphology of lateral-line canal system of the genera *abramis*, *blicca* and *vimba* with regard to their ecology and systematic position. *Acta Univ. Carol. Biol.* **12**, 105–153.

Jamieson, A. J., Fujii, T., Solan, M., Matsumoto, A. K., Bagley, P. & Priede, I. G. 2009*a* Liparid and macrourid fishes of the hadal zone: *in situ* observations of activity and feeding behaviour. *Proc. R. Soc. B* **276**, 1037–1045. (doi:10.1098/rspb.2008.1670)

Jamieson, A. J., Solan, M. & Fujii, T. 2009*b* Imaging deep-sea life beyond the abyssal zone. *Sea Technol.* **50**, 41.

Julier, S. J. & Uhlmann, J. K. 2004 Unscented filtering and nonlinear estimation. *Proc. IEEE* **92**, 401–422. (doi:10.1109/JPROC.2003.823141)

Krantz, S. G. 1999 Special classes of holomorphic functions. In *Handbook of complex variables*, ch. 12, pp. 149–154. Basel, Switzerland: Birkhäuser.

Liao, J. C. 2006 The role of the lateral line and vision on body kinematics and hydrodynamic preference of rainbow trout in turbulent flow. *J. Exp. Biol.* **209**, 4077–4090.

Liao, J. C. 2007 A review of fish swimming mechanics and behaviour in altered flows. *Phil. Trans. R. Soc. B* **362**, 1973–1993. (doi:10.1098/rstb.2007.2082)

McConney, M. E., Chen, N., Lu, D., Hu, H. A., Coombs, S., Liu, C. & Tsukruk, V. V. 2009 Biologically inspired design of hydrogel-capped hair sensors for enhanced underwater flow detection. *Soft Matter* **5**, 292–295. (doi:10.1039/b808839j)

Milne-Thomson, L. M. 1968 *Theoretical hydrodynamics*, 5th edn. New York, NY: MacMillan.

Montgomery, J. C., Baker, C. F. & Carton, A. G. 1997 The lateral line can mediate rheotaxis in fish. *Nature* **389**, 960–963.

Montgomery, J. C., Coombs, S. & Baker, C. F. 2001 The mechanosensory lateral line system of the hypogean form of *astyanax fasciatus*. *Environ. Biol. Fishes* **62**, 87–96.

Montgomery, J. C., Macdonald, F., Baker, C. F. & Carton, A. G. 2002 Hydrodynamic contributions to multimodal guidance of prey capture behavior in fish. *Brain Behav. Evol.* **59**, 190–198. (doi:10.1159/000064906)

Morse, P. M. & Feshbach, H. 1953 *Methods of theoretical physics*, vol. I. New York, NY: McGraw-Hill.

Muskhelishvili, N. I. 1963 *Some basic problems of the mathematical theory of elasticity fundamental equations, plane theory of elasticity, torsion and bending*. Gröningen, The Netherlands: P. Noordhoff Ltd.

Nehari, Z. 1952 *Conformal mapping*. New York, NY: Dover.

Nelson, M. E. & MacIver, M. A. 2006 Sensory acquisition in active sensing systems. *J. Comp. Physiol. A* **192**, 573–586. (doi:10.1007/s00359-006-0099-4)

Nelson, M. E., MacIver, M. A. & Coombs, S. 2002 Modeling electrosensory and mechanosensory images during the predatory behavior of weakly electric fish. *Brain Behav. Evol.* **59**, 199–210. (doi:10.1159/000064907)

Pólya, G. & Szegö, G. 1951 *Isoperimetric inequalities in mathematical physics*. Princeton, NJ: Princeton University Press.

Pommerenke, C. 1975 *Univalent functions*. Göttingen, The Netherlands: Vandenhoeck & Ruprecht.

Rapo, M. A., Jiang, H., Grosenbaugh, M. A. & Coombs, S. 2009 Using computational fluid dynamics to calculate the stimulus to the lateral line of a fish in still water. *J. Exp. Biol.* **212**, 1494–1505. (doi:10.1242/jeb.026732)

Rothe, I., Susse, H. & Voss, K. 1996 The method of normalization to determine invariants. *IEEE Trans. Pattern Anal. Mach. Intell.* **18**, 366–376. (doi:10.1109/34.491618)

Sharon, E. & Mumford, D. 2006 2D-shape analysis using conformal mapping. *Int. J. Comput. Vision* **70**, 55–75. (doi:10.1007/s11263-006-6121-z)

Sichert, A. B., Bamler, R. & van Hemmen, J. L. 2009 Hydrodynamic object recognition: when multipoles count. *Phys. Rev. Lett.* **102**, 058104. (doi:10.1103/PhysRevLett.102.058104)

Triantafyllou, M. S., Triantafyllou, G. S. & Yue, D. K. P. 2000 Hydrodynamics of fishlike swimming. *Annu. Rev. Fluid Mech.* **32**, 33–53. (doi:10.1146/annurev.fluid.32.1.33)

Tsuji, M. 1959 *Potential theory in modern function theory*. Tokyo, Japan: Maruzen Co. Ltd.

von Campenhausen, C., Riess, I. & Weissert, R. 1981 Detection of stationary objects by the blind cave fish *anoptichtys jordani* (characidae). *J. Comp. Physiol.* **143**, 369–374.

Windsor, S., Tan, D. & Montgomery, J. 2008 Swimming kinematics and hydrodynamic imaging in the blind mexican cave fish (*Astyanax fasciatus*). *J. Exp. Biol.* **211**, 2950–2959. (doi:10.1242/jeb.020453).

Yang, Y. C., Chen, J., Engel, J., Pandya, S., Chen, N. N., Tucker, C., Coombs, S., Jones, D. L. & Liu, C. 2006 Distant touch hydrodynamic imaging with an artificial lateral line. *Proc. Natl Acad. Sci. USA* **103**, 18 891–18 895. (doi:10.1073/pnas.0609274103)